Title
MEASUREMENT OF n+ -He SCATTERING AND ITS RELATION TO THE PION FORM FACTOR

Authors
Crowe, Kenneth M.
Fainberg, Anthony
Miller, Jacques
et al.

Publication Date
1968-09-01

UCRL-18473

Cy. 2

MEASUREMENT OF $\pi^{\pm}$-He SCATTERING AND ITS RELATION TO THE PION FORM FACTOR

Kenneth M. Crowe, Anthony Fainberg, Jacques Miller,
and Anthony S. L. Parsons

September 1968

LAWRENCE RADIATION LABORATORY
UNIVERSITY of CALIFORNIA BERKELEY

Cy. 2

UCRL-18473

34

DISCLAIMER

Submitted to Physical Review

UCRL-18473
Preprint

UNIVERSITY OF CALIFORNIA

Lawrence Radiation Laboratory
Berkeley, California

AEC Contract No. W-7405-eng-48

MEASUREMENT OF $\pi^{\pm}$ - He SCATTERING AND ITS RELATION TO THE PION FORM FACTOR

Kenneth M. Crowe, Anthony Fainberg, Jacques Miller,
and Anthony S. L. Parsons

September 1968

MEASUREMENT OF $\pi^{\pm}$ - He SCATTERING AND ITS RELATION TO THE PION FORM FACTOR*

Kenneth M. Crowe, Anthony Fainberg, Jacques Miller,† and Anthony S. L. Parsons

Lawrence Radiation Laboratory
University of California
Berkeley, California

September 1968

Abstract

A measurement has been made of the differential cross section for the elastic scattering of positive and negative pions of energies 51, 60, 68, and 75 MeV scattered from helium. The experiment is discussed and a phase-shift analysis is presented. An optical-model analysis has been used to extract the pion electromagnetic radius, yielding 2.96 ± 0.43 F. There remain uncertainties in this application of the model, which are discussed.

Introduction

We present here a measurement of the elastic scattering processes $\pi^{\pm} + \alpha \rightarrow \pi^{\pm} + \alpha$, with a phenomenological analysis of our results. The experiment was performed in an effort to obtain the pion electromagnetic form factor. Our theoretical analysis is based on an optical model and follows that suggested by Auerbach et al.[1]

Hofstadter and Sternheim originally proposed[2] that the pion charge form factor can be obtained by the analysis of charge asymmetry in pion-helium scattering. The first experiment by Nordberg and Kinsey,[3] using 24-MeV pions, obtained $R_{\pi} = 1.8 \pm 0.8$ F. However, Schiff pointed out[4] the importance of distortion effects in the analysis of this experiment, and a recalculation based on an optical model to compute the distortion[1,5] leads to a modification of this result, $R_{\pi} < 2.0$ F (2 s.d.). Block et al.,[6] interpreting their helium bubble chamber data at several energies, obtained the results $R_{\pi} < 0.9$ F (1 s.d.) or < 2.1 F (2 s.d.). Auerbach et al. have presented[1] a detailed discussion of the optical model as applied to the problem. Ericson has pointed out[7] the advantage of using the difference in the S-state phase shift where the major size dependence occurs. Berman[8] and others have criticized the interpretation of the experiment, especially with regard to the existence of certain model-dependent distortion effects, which are neglected in this analysis. These effects arise from the fact that the amplitude for our process contains contributions from relativistic effects which have not to our knowledge been calculated (see part D of Analysis).

Our analysis gives $R_{\pi} = 2.96 \pm 0.43$ F. Two other experimental techniques have been used in attempts to measure R_{π}. From the

scattering of pions off atomic electrons, Cassel et al.[9] were only able to assign a limit of $R_\pi < 3.0$ F. This method is limited by the small value of momentum transfer obtainable using present pion beam energies. Another phenomenological analysis using electroproduction has been used in two experiments. Akerlof et al.[10] find $R_\pi = 0.80 \pm 0.10$ F, and Mistretta et al.[11] obtain $R_\pi = 0.86 \pm 0.14$ F. The vector-meson dominance model predicts an rms radius of ≈ 0.6 F.

Experimental Description

A pion beam of 90 MeV obtained from an internal target of the 184-inch Berkeley Synchrocyclotron is shown schematically in Fig. 1. Negative pions produced in the forward direction at the target were accepted by the transport system. Positive pions (produced in the backward direction) were obtained in the same beam line by reversing the cyclotron main field. Consideration of sensitivity to the pion form factor leads to an optimum energy for the measurement of about 60 MeV for the incident pions;[12] here (at the minimum in the nuclear cross section) a sufficiently large value of momentum transfer is obtained and the interference between the Coulomb and nuclear amplitudes is significant. The beam was degraded at an intermediate focus. The momentum band of $\pm 3\%$ was essentially the same for all energies.

Time-of-flight counters (TOF 1 and TOF 2) were used to reject electrons or positrons in the beam (about 25% for electrons and 5% for positrons) that would otherwise introduce an asymmetry in the beam normalization. The time resolution was set to include the muons from pion decay, which were approximately 15% of the flux; the correction for

muons is described below. The direction of the incident pion in the horizontal plane and the spatial distribution of pions at the target were defined by hodoscope A (11 counters, 1.9 cm wide, 0.63 cm thick) and B (5 counters, 1.9 cm wide, 0.63 cm thick). Two further beam-defining counters were used for calibration purposes. A lead opening 10 cm long was situated about 30 cm from the target with a 7.6 × 7.6-cm aperture to reduce the flux of particles incident on the walls of the target and the vacuum jacket. The target itself consisted of a 7.6-cm-diameter vertical cylinder of liquid helium.

Scattered pions were detected in an array of 16 scintillation counter telescopes each consisting of three counters placed respectively 30.5, 86.4, and 101.7 cm from the target, as shown in Fig. 1. These telescopes were mounted in such a way that they could be rotated about the target; this facility allowed each telescope to be set in the primary beam for efficiency measurement. Also, the telescopes were used to make measurements at several angles. The most interesting region, from 60 to 80 deg, was covered by 10 of the telescopes, 5 on either side of the beam. The remainder spanned the other angles between 30 and 150 deg. The dimensions of the counters were 2.54 cm wide, 1.27 cm thick, and either 30.5 or 50.8 cm long, the longer type covering the angular interval 60 to 100 deg, where the contributions to the angular resolution due to the length of the counters is small.

The two contaminants among the scattered particles were inelastically scattered pions, and protons arising from pion capture. The inelastic pions were rejected by a range requirement in the telescopes. At each angle, range curves were obtained and sufficient range (consisting

of slabs of CH_2) was inserted to reject the inelastic pions, which have at least 20 MeV less energy than those elastically scattered. A typical range curve is shown in Fig. 2.

Protons were rejected by use of pulse-height information as follows. Information on which of the counters fired for any one event in the telescope and hodoscope arrays was stored in a PDP5 computer, and on tape, for subsequent analysis on the CDC 6600.

The trigger for an event was a beam-particle trigger plus a scattered-particle trigger. The former was defined by a time of flight within the appropriate gate as well as by the two hodoscopes; the latter required all three telescope counters.

At the time of an event trigger, the pulse height obtained from the output of the first telescope counter was stored in the computer. The separation of pions and protons was essential, since the protons from the capture process, if counted to any significant extent, could introduce a marked asymmetry between π^- and π^+ cross sections. The probability of capture of a pion in nuclear matter on two unlike nucleons is several times that for like nucleons, which gives rise to an observed ratio of energetic proton yields from helium of about 18 to 1 for π^+ and π^- capture respectively. To allow for the slight overlap of the pulse-height spectra for each telescope, each run was fitted by an expression which was the sum of two Gaussian distributions; the total area under the peaks was constrained to be the total number of counts in that telescope, but the ratios of the areas of the peaks, their positions, and their widths were allowed to be free parameters. Examples of pulse-height spectra are shown in Fig. 3.

During the runs, many checks on the consistent behavior of the counters, on the electronics, and on the pion beam itself were made. Most of these checks were monitored by the on-line computer. The important accidental coincidence rates were also monitored.

Checks on the efficiency of each telescope were made by rotating each into the primary beam (0-deg direction) and measuring the ratio of telescope counts registered in the computer to the number of coincidences between three additional counters--these coincidences defined a pion as having passed through all three telescope counters.

The method of running was typically to spend about 1 hour with the target full (about 10^4 events) and then 0.5 hour with the target empty, followed by about 5 minutes triggering the computer only on a beam particle; this last type of run provided a random sample for measuring the angular and spatial distribution of the beam at the target as well as a monitor on the probability of random counts in the telescope counters. The signal-to-background ratio was typically 10:1 at backward angles and about 2:1 around the minimum in the cross section.

Several corrections were applied to the data, both to the number of scattered pions at a given angle and to the intensity of the incident beam. Those corrections are summarized in Table I, and the important ones are discussed below. It should be noted that several of the corrections are the same for both the positive and negative cross-section measurements.

The main correction to the incident beam intensity was for the muon contamination. This was calculated by using a Monte Carlo type program simulating the transport of pions from the cyclotron internal

target to the helium target and including π-μ decay in flight. The predicted range curves and time-of-flight spectra were compared with those obtained experimentally and were found to be in good agreement. The fraction of muons varied from 20 ± 3% at 51 MeV to 12 ± 2% at 75 MeV.

The other correction to the incident flux was the random coincidence between an electron or positron in the counters immediately ahead of the target and another particle counting in the upstream time-of-flight counter (TOF). This correction amounted to about 3% with less than 1% difference between the two signs of beam.

The major correction to the number of scattered pions is the loss due to multiple scattering in the target, counters, and range. This correction was computed for each angle with a Monte Carlo program including energy loss of the particles and π-μ decay, as well as the scattering process. The error of 1.5% in this correction arose from the statistical nature of the Monte Carlo process. Nuclear scattering and absorption were estimated by using the data of Stork[13] and Byfield[14] as well as data obtained in the beam in this experiment, both sources of information being essentially in agreement; the error of 2% in this figure is an estimate from the published data.

Data for each sign of particle were obtained at 51, 60, 68, and 75 MeV. The correction for the protons arising from π^- capture was measured to be 5% at 60 MeV. The corrections at other momenta were made by assuming that the ratio of the proton yields from π^+ and π^- capture is constant with energy.

As a check on the whole setup, some data were obtained at 60 MeV, with hydrogen used in the target. For these measurements the absorbing

ranges were removed from the telescopes. These data are shown in Fig. 4, compared with the predictions of the most recent πp phase-shift analysis.[15] The agreement is reasonable considering the precision, in this region, of the data upon which the phase-shift analysis is based.

Analysis

Figure 5 shows $\frac{d\sigma^-}{d\Omega}_{c.m.}$, $\frac{d\sigma^+}{d\Omega}_{c.m.}$, and $\frac{d\sigma\,(av)}{d\Omega}_{c.m.}$.

The difference in the cross sections divided by the average ($= D/A$) is shown in Fig. 6. This variable is sensitive to R_π because the nuclear amplitude cancels to first order and because it is independent of those correction factors which are the same for π^- and π^+. The sensitivity to R_π is shown for 60 MeV. The data in the form of differential cross sections versus $\theta_{c.m.}$ are presented in Table II.

A phase-shift analysis has been made up to the D wave. Higher partial waves are not significant. The phase shifts are shown in Table III. The total inelastic cross-section data of Block et al.[6] are used to constrain the imaginary parts of the phase shifts.

Two methods, described below, have been used to extract the pion radius.

A. The Optical Potential Method

In this method a particular potential is postulated for the strong interaction. Following the method of Auerbach et al.,[1] a Kisslinger model[16] is used for the form of the potential. The modified Klein-Gordon equation

$$(-\nabla^2 + \mu^2)\,\psi = [(E_\pi - V_c)^2 - U]\,\psi$$

is solved, where E is the total c.m. energy of the pion, μ is the reduced mass, and V_c is the Coulomb potential. The optical potential, U, is defined by

$$U\psi = [-Ab_0 k^2 \rho_N(r) + Ab_1 \vec{\nabla} \cdot \{\rho_N(r) \vec{\nabla}\}] \psi,$$

with A the number of nucleons, b_0 and b_1 the complex optical parameters which are introduced to represent the s- and p-wave πN scattering, respectively, and $\rho_N(r)$ the nuclear density. To allow for the recoil of the α particle and provide for relativistic kinematics, a modification[17] of the expression of Goldberger and Watson[18] is used:

$$(\nabla^2 + k^2) \psi = (2 E_{eq} V_c + (1 - 3 E_{eq}/W) V_c^2 - U)\psi, \qquad (1)$$

where E_{eq} is the equivalent relativistic one-particle c.m. energy, W is the total c.m. energy, and k is the c.m. momentum.[19]

This equation is solved for the radial wave functions. Given b_0, b_1, E_{eq}, $\rho_N(r)$, and V_c, cross sections are obtained for the solutions by matching logarithmic derivatives at the nuclear surface to the external Coulomb wave functions in the conventional way. For a given energy, then, there are six parameters which lead to predicted cross sections: the real and imaginary parts of b_0 and b_1, and radius parameters for $\rho_N(r)$ and for $\rho_c(r)$. A Gaussian form is taken both for the nuclear density $\rho_N(r)$ and the combined π-He charge density $\rho_c(r)$: $\rho_N(r) = A \exp(-r^2/a^2)/[(\pi)^{1/2} a]^3$ and $\rho_c(r) = Ze \exp(-r^2/R_c^2)/[(\pi^{1/2} R_c]^3$. The Coulomb radius parameter is related to the rms radius of the pion by $R_\pi^2 = 1.5 R_c^2 - R_{He}^2$, with $R_{He} = 1.65 \pm .03$ F, from electron scattering experiments.[20,21]

An optimum set of parameters is found by searching for the best fit to the data. A fit is made simultaneously to the average cross section and to the D/A data.

The parameters b_0, b_1, a, and R_c obtained by this direct method of fitting the data with an optical model are listed in Table IV.[22] The errors quoted are derived from the diagonal elements of the error matrix shown in Table V. R_c's diagonal element is sufficiently larger than its off-diagonal elements so that the error quoted for R_c, and consequently for R_π, is, we believe, reliable. The errors on the parameters in the table also include uncertainties in absolute and relative $\pi^- - \pi^+$ normalization.

The values of χ^2 obtained by using statistical errors only for the best fits are somewhat larger than expected from the numbers of degrees of freedom. In propagating the errors of the data to include systematic errors, we have increased the estimate of the errors by an appropriate factor $(\chi^2/\chi^2_{\text{expected}})^{1/2}$. The fits to the D/A data are better than those for the average, since some systematic errors in the experimental corrections made for a particular angle would cancel in D/A.

A problem in this analysis has been pointed out by Baker et al.[23] The radial wave equation arising from (1) is

$$\frac{d^2\chi_\ell}{dr^2} + p(r)\,\frac{d\chi_\ell}{dr} + q(r)\,\chi_\ell = 0,$$

where $p(r) = \dfrac{2}{r} + \dfrac{\dfrac{d\rho_N(r)}{dr}}{1+Ab_1\rho_N(r)}$

$$\text{and } q(r) = \frac{k^2 - Ab_0 \rho_N(r) - 2E_{eq} V_c - (1-3E_{eq}/W) V_c^2}{1 + Ab_1 \rho_N(r)} - \frac{\ell(\ell+1)}{r^2} .$$

Because of the term $1 + Ab_1 \rho_N(r)$ in the denominators of the coefficients, there is a regular singular point in the equation when $Ab_1 \rho_N(r) = -1$.[24]

Since A and $\rho_N(r)$ are real, the denominator factor, $1 + Ab_1 \rho_N(r)$, induces a logarithmic branch point in the radial wave function, for $Reb_1 = -1/A\rho_N(r)$ and $Imb_1 = 0$. For the Imb_1 small, the singularity becomes a sharp peak. The presence of the singularity means that certain regions of the optical parameter space are forbidden implicitly by the model.[25] Because of the coupling between Imb_0 and Imb_1, in fitting our data, the above restriction on Imb_1 forces Imb_0 to a slightly positive value, which violates unitarity.[26]

B. The Phase-Shift Method

Another method of analysis uses the optical model only to calculate the distortion amplitudes. The phase-shift analysis is used to obtain amplitudes for π^+ and π^- scattering.

If one writes the total amplitude as the sum of a nuclear amplitude, f^N, a distortion amplitude, f^D, and the point Coulomb amplitude, f^{pt}, the total cross section is

$$\frac{d\sigma\pm}{d\Omega} = \left| f^N \pm f^D \pm F f^{pt} \right|^2 .$$

This equation is solved to find the form factor, F, for each data point at each energy, giving

$$F = A + B, \qquad (2)$$

where $A = \left(\frac{d\sigma+}{d\Omega}_{c.m.} - \frac{d\sigma-}{d\Omega}_{c.m.} \right) / 4 \text{ Re } f^{N*} f^{pt}$

and $B = -4 \text{ Re } f^{N*} f^{D} / 4 \text{ Re} f^{N*} f^{pt}$.

The measured quantity is A and the distortion effect is B. Where $A >> B$, the distortion effect is negligible.

The distortion amplitude is calculated following Auerbach.[1,27] In Fig. 7, -A and B vs $\cos\theta_{c.m.}$ for 60 MeV are shown. This figure shows that f^D is extremely important in determining F. Combining all the data for the various energies, we can plot $F_\pi(q^2)$ vs q^2 (Fig. 8a). Assuming a Gaussian charge distribution for the helium and pion $F = \exp(-q^2R^2/6)$ with $R^2 = R_\pi^2 + R_{He}^2$, we fit the $F_\pi(q^2)$ to find R_π. The result is 2.96±0.43 F. In assigning the error the same χ^2 factor mentioned in part A is used.

This error does not include the uncertainty in the form factor due to the error in the relative normalization of the π+ and π- data. This is displayed in Fig. (8a). Figure (8b) shows the radius computed independently for each $F_\pi(q^2)$ data point with different relative normalizations. It is noted that below 1 F^{-2} the radius shows only slight sensitivity to the relative normalization. In fact, for all data points the best fit to $F_\pi(q^2)$ is almost independent of the relative normalization. At $q^2 > 1$ F^{-2} the larger fluctuations are a consequence of the insensitivity of D/A to R_π in this region (see Fig. 6). The normalization error in Table I common to both signs of beam has a negligible effect on the form factor.

This method can, in principle, be used to show the consistency of the form-factor measurement at different energies. In this measurement the statistics are not sufficiently accurate for this check to be made.

C. Distortion Amplitudes by Other Methods

It is interesting to compare our distortion amplitudes with those arrived at by using other approximate calculations of f^D. West[5] obtains

$$f_\ell^D = -\int V_c(r)\left[e^{2i\delta_\ell} R_\ell^2(r) - j_\ell^2(kr) - (e^{2i\delta_\ell}-1)/2k^2 r^2\right] r^2\, dr,$$

where $V_c(r) = \frac{4nk}{\pi}\int_0^\infty F_\pi(q^2)\, F_\alpha(q^2)\, j_0(qr)\, dq$, with a Yukawa form for F_π and a square-well density leading to $F_\alpha = 3\, j_1(qb)/qb$. Here, b is the radius of the square well. The nuclear radial wave function is R_ℓ and the nuclear phase shift is δ_ℓ. To evaluate R_ℓ West has chosen a square well; the Kisslinger model is modified by substituting $[1 - Ab_1\rho_N(r)]$ for $[1 + Ab_1\rho_N(r)]^{-1}$, following Baker et al.[23]

Block[6] obtains for the distortion amplitude another approximation,

$$f_\ell^D = \left[nx_\ell\, e^{2i\delta_\ell} + (e^{2i\delta_\ell}-1)(\eta_\ell - \eta_0)\right]/k,$$

where an additional term of the form $(e^{2i\delta_\ell}-1)\, 2n \log[1/2(1-\cos\theta)]/k$ is neglected, and where $nx_\ell = -k\int V_c(r)[R_\ell^2(r) - j_\ell^2(kr)]\, r^2 dr$ and η_ℓ are the Coulomb parameters defined by $\eta_\ell = \arg\Gamma(\ell + 1 + in)$ and $n = ZZ'e^2/\hbar v_{relative}$. Here, $V_c(r) = \frac{2nk}{r}\,\mathrm{erf}(r/R_c)$. Block's R_ℓ is found by using a local potential for each partial wave and a Gaussian distribution for both the nuclear and Coulomb interactions. The results for 60 MeV obtained from these equations are also presented in Table VI for comparison; the distortion amplitudes obtained by Block et al.[6] from the bubble chamber data are shown.

Ericson has shown[7] that all the information on the pion charge radius is in the s wave, due primarily to the s-wave overlap of the pion with the

nucleus. Since the imaginary part of f^{pt} is negligible, $\mathrm{Re}\, f^{D}_{\ell=0}$ is the important distortion amplitude to determine. It will be noted that $\mathrm{Re}\, f^{D}_{\ell=0}$ differs in sign according to the method used. The corresponding radii computed by the phase-shift method (except for Block's data, where his radius for all his energies is quoted) are shown for each set of distortion amplitudes.

D. Discussion

There are some deficiencies in the optical-potential description as applied to this problem.

Firstly, although it may provide a good phenomenological fit to pion-nucleus scattering data in the sense that it attempts to include the strong p-wave π-nucleon scattering, the model itself may not be sufficient to calculate the distortion amplitudes to the accuracy required in this measurement. Secondly, as emphasized in the introduction, the optical potential is a nonrelativistic description of the π-He interaction. Specifically, diagrams of the type shown in Fig. 9 are neglected;[8,28] such diagrams are clearly of importance for our purposes, since their amplitudes are linear in the pion charge, and a fundamental assumption in our analysis is that the only terms of this type are the pure Coulomb and the Coulomb-nuclear distortion terms. Electrodynamic corrections of this nature involving strong interactions have not been calculated to our knowledge. In this connection we remark that since the pion form factor effect is at most 10% in the differential cross section, violation of charge symmetry in the strong interaction at a relatively low level would be serious from our point of view. However, in a recent review, Henley[29] sets an upper limit of 0.8% on charge-symmetry violation in hadronic forces; this would correspond to less than 0.05 F in the pion radius.

Conclusion

The $\pi^{\pm}$ - He elastic differential cross section has been measured at several energies and phase shifts evaluated. In attempting to extract the pion electromagnetic radius from the difference in the cross sections, the most detailed model available for describing the pion nucleus interaction has been used, yielding $R_{\pi} = 2.96 \pm 0.43$ F. This result is clearly inconsistent with the vector meson dominance model and with measurements of R_{π} using electroproduction. Some inadequacies in the model have been emphasized, particularly in relation to its nonrelativistic nature.

Acknowledgments

It is a pleasure to acknowledge many illuminating conversations with Dr. T. Ericson, Professor R. Hofstadter, Mr. C. Thomas Mottershead, Professor Robert Riddell, Professor L. Schiff, Professor Morton Sternheim, and Dr. Joel Yellin. Also, we thank Mr. Norman Gunther for his invaluable programming assistance, and the many other programmers and technicians who helped in the experiment. We especially extend our thanks to Mr. Leonard Proehl, whose expertise with the electronics was a great help.

Finally, we express our sincere appreciation to Mr. James Vale and the crew of the 184-inch synchrocyclotron.

Footnotes and References

*Work done under auspices of the U. S. Atomic Energy Commission.

†Present address: Centre d'Études Nucléaires, Saclay, France.

1. E. H. Auerbach, D. M. Fleming, and M. M. Sternheim, Phys. Rev. 162, 1683 (1967).
2. M. M. Sternheim and R. Hofstadter, Nuovo Cimento 38, 1854 (1965).
3. M. E. Nordberg, Jr., and K. F. Kinsey, Phys. Letters 20, 692 (1966).
4. L. I. Schiff, Progr. Theor. Phys. Supplement 400 (1965).
5. G. B. West, Phys. Rev. 162, 1677 (1967).
6. M. M. Block, I. Kenyon, J. Keren, D. Koetke, P. Malhotra, R. Walker, and H. Winzeler, Phys. Rev. 169, 1074 (1968).
7. M. Ericson, Nuovo Cimento 47, 49 (1967).
8. S. N. Berman (Stanford University), private communication.
9. D. G. Cassel (Thesis), NP-14885, Princeton, 1965.
10. C. W. Akerlof, W. W. Ash, K. Berkelman, C. A. Lichtenstein, A. Ramanauskas, and R. H. Siemann, Phys. Rev. 163, 1482 (1967).
11. C. Mistretta, D. Imrie, J. A. Appel, R. Budnitz, L. Carroll, M. Goitein, K. Hanson, and Richard Wilson, Phys. Rev. Letters 20, 1523 (1968).
12. E. H. Auerbach, D. M. Fleming, and M. M. Sternheim, Brookhaven Laboratory Report BNL-12309, 1968.
13. D. H. Stork, Phys. Rev. 93, 868 (1954).
14. H. Byfield, Phys. Rev. 86, 17 (1952).
15. A. Donnachie, R. G. Kirsopp, and C. Lovelace, CERN Report TH-838 1967.
16. L. S. Kisslinger, Phys. Rev. 98, 761 (1955).

17. This modification was derived by C. T. Mottershead.

18. M. L. Goldberger and K. M. Watson, Collision Theory (John Wiley and Sons, Inc., New York, 1964), p. 340.

19. For 60 MeV, E_{eq} = 184.7 MeV, compared with $E_{\pi_{c.m.}}$ = 194.2 MeV. If $E_{\pi_{c.m.}}$ is used in the optical-model analysis, and the recoil is neglected, the final answer for the radius of the pion is larger by 10% for this method of analysis.

20. H. Frank, D. Haas, and H. Prange, Phys. Letters 19, 391, 719 (1965).

21. G. R. Burleson and H. W. Kendall, Nucl. Phys. 19, 68 (1960).

22. The inclusion of the Lorentz-Lorenz effect involves replacing $b_1\rho(r)$ by $b_1\rho(r)/[1-\frac{1}{3}b_1\rho(r)]$. See M. Ericson and T. E. O. Ericson, Ann. Phys. 36, 326-362 (1966). When this is done in the search routine, the optical parameters change slightly, but R_c varies only by about 3%.

23. W. F. Baker, H. Byfield, and J. Rainwater, Phys. Rev. 112, 1773 (1958).

24. E. T. Whittaker and G. N. Watson, Modern Analysis (Macmillan Company, New York, 1947), p. 197-201.

25. C. T. Mottershead (Lawrence Radiation Laboratory), private communication.

26. We thank Dr. Joel Yellin for enlightening conversations on this question, which is being further investigated.

27. We write

$$f^{\pm} = [\Sigma (2\ell+1)(f_\ell{}^N \pm f_\ell{}^D \pm f_\ell{}^{size}) P_\ell(\cos\theta)] \pm f^{pt}$$

$$= \Sigma (2\ell+1)\, f_\ell{}^{\pm}(\cos\theta) \pm f^{pt},$$

where the amplitude $f_\ell{}^D$ is defined to be the distortion amplitude in the ℓth partial wave; if the strong interaction vanishes, it disappears. The amplitudes f^{size} arise from the deviation from a point-charge distribution and are purely Coulomb; f^{pt} is the point-charge amplitude,

$$f_\ell{}^N = \frac{(f_\ell{}^+ + f_\ell{}^-)}{2},$$

and

$$\Sigma (2\ell+1)\, f_\ell{}^{size} P_\ell(\cos\theta) = (F-1) f^{pt},$$

where F is the product of the electromagnetic form factors for the helium and the pion. The amplitudes $f_\ell{}^D$ are found by solving Eq. (1) with and without strong interactions, using

$$f_\ell{}^D = \frac{(f_\ell{}^+ - f_\ell{}^- - f_\ell{}^{size})}{2}.$$

Although $f_\ell{}^{size}$ varies with the charge radius, we find $f_\ell{}^D$ to be almost independent of this input, and this small variation in $f_\ell{}^D$ is included in assigning its error as are the various sensitivities of $f_\ell{}^D$ to changes in each of the optical parameters.

28. J. Rix and R. M. Thaler, Phys. Rev. 152, 1357 (1966).

29. E. M. Henley, Charge Independence and Charge Symmetry of Nuclear Forces, to be published in Isospin in Nuclear Physics.

Table I. Corrections applied to the new data.

Description of measurement or correction	Source of estimate	Approximate amount of correction (%)	Approximate error in measurement or correction (%)
CORRECTIONS TO AND MEASUREMENTS OF BEAM INTENSITY:			
1. Number of beam particles	Scaled at 100 mHz	---[a]	
2. μ fraction	(i) Monte Carlo (ii) Range + time-of-flight measurements	-15	3
3. Randoms	Measured experimentally	3	1.5
4. Dead time	Measured experimentally	< 1	
CORRECTIONS TO AND MEASUREMENTS OF NUMBER OF PIONS SCATTERED:			
1. Number of pions	Scaled	---	2 (statistical)
2. Solid-angle measurement	From counter position survey	---	1.0
3. Multiple scattering in target + counters + range	Monte Carlo	+10 [a]	±1.5
4. π-μ decay		+15 [a]	
5. μ's detected from π-μ decay		- 5 [a]	
6. Nuclear absorption and scattering in counters and range	(i) $\sigma_{inelastic}$ and $\sigma_{elastic}$ data (ii) measurements in beam	+ 7 [a]	2 (exptl. errors)
7. μ's Coulomb scattering in ^{4}He	Calculated	2 at forward angles [a]	<0.5
8. Inefficiency of counters	Measured frequently during expt.	<1	<0.5
9. Contamination by protons from π capture	Distinguished by pulse height	---	---
10. Correction due to two C counters firing	From "beam triggered" runs	1 to 2 [a]	<0.5

a. Cancels for D/A.

UCRL-18473

Table II. Data for each of the four energies in the form of differential cross sections as a function of $\theta_{c.m.}$

$\theta_{c.m.}$ (deg)	$\frac{d\sigma+}{d\Omega}$ (mb/sr)	ϵ_+ (mb/sr)	$\frac{d\sigma+}{d\Omega}$ (mb/sr)	ϵ_- (mb/sr)
51 MeV				
31.5	1.516	0.140	5.192	0.254
36.7	1.611	0.136	3.969	0.166
41.9	1.223	0.093	2.978	0.145
47.1	1.131	0.093	2.033	0.107
62.5	0.434	0.024	0.560	0.025
67.6	0.266	0.023	0.371	0.020
72.7	0.323	0.020	0.269	0.019
77.8	0.375	0.023	0.314	0.020
82.8	0.581	0.026	0.427	0.023
92.9	0.993	0.050	0.950	0.041
102.8	1.610	0.057	1.638	0.053
122.5	3.433	0.144	3.715	0.132
132.2	4.095	0.164	4.471	0.148
141.8	4.764	0.177	4.791	0.147
151.4	4.918	0.194	5.034	0.156
60 MeV				
31.5	2.661	0.075	6.712	0.146
36.7	2.634	0.071	5.033	0.106
41.9	2.327	0.052	3.854	0.076
47.1	1.663	0.046	2.835	0.062
62.6	0.534	0.010	0.747	0.013
67.7	0.366	0.009	0.436	0.009
72.8	0.325	0.008	0.306	0.008
77.9	0.375	0.008	0.336	0.009
83.0	0.618	0.012	0.521	0.011
93.0	1.128	0.021	1.077	0.021
102.9	1.928	0.031	1.916	0.031
122.6	3.936	0.079	4.232	0.083
132.3	4.592	0.104	4.875	0.109
141.9	5.422	0.150	5.544	0.153
151.5	5.721	0.196	5.924	0.203
68 MeV				
31.6	4.031	0.190	7.299	0.273
36.8	3.612	0.176	5.312	0.361
42.0	3.247	0.135	4.494	0.164
47.2	2.651	0.126	3.082	0.223
62.7	0.722	0.025	0.925	0.034
67.8	0.437	0.020	0.512	0.026
72.9	0.382	0.018	0.366	0.022
78.0	0.447	0.019	0.388	0.025
83.1	0.692	0.025	0.556	0.030
93.1	1.350	0.047	1.180	0.051
103.0	2.094	0.063	2.018	0.069
122.7	4.011	0.149	4.392	0.142
132.4	4.961	0.176	5.098	0.163
142.0	5.853	0.213	5.543	0.316
151.5	5.843	0.267	5.591	0.333
75 MeV				
31.6	5.940	0.205	9.394	0.236
36.9	5.252	0.167	7.080	0.215
42.1	4.268	0.141	5.858	0.132
47.3	3.006	0.104	3.979	0.127
62.8	0.960	0.025	1.119	0.023
67.9	0.623	0.019	0.667	0.017
73.0	0.458	0.017	0.488	0.014
78.1	0.529	0.019	0.498	0.015
83.2	0.776	0.023	0.710	0.018
93.2	1.413	0.042	1.325	0.035
103.1	2.203	0.057	2.361	0.050
122.8	4.508	0.143	4.578	0.103
132.4	5.264	0.152	5.379	0.116
142.0	6.054	0.175	5.646	0.169
151.6	6.114	0.200	6.046	0.203

Table III. Phase shifts (degrees)

Energy (MeV)		ReS	ImS	ReP	ImP	ReD	ImD
51	π^+	- 7.5±.5	1.6±1.8	9.0±.2	2.2±1.4	1.0±.1	.2±.3
	π^-	- 9.3±.2	1.9±1.2	9.1±.2	2.4±1.3	1.0±.2	.1±.1
60	π^+	- 8.0±.5	2.9± .8	11.4±.3	1.4±1.0	1.6±.1	.3±.3
	π^-	-10.4±.3	2.0±1.2	11.4±.5	3.3±1.8	1.4±.1	.7±.4
68	π^+	- 8.6±.5	1.7± .8	13.4±.5	3.7± .7	2.1±.1	.6±.2
	π^-	-11.0±.5	2.4±1.8	12.8±.5	4.1±2.0	1.7±.2	.8±.1
75	π^+	- 7.9±1.4	.1±1.6	15.5±.5	7.2±1.8	2.8±.3	.6±.5
	π^-	-10.7± .9	1.6±2.2	15.2±.5	6.2±3.3	2.7±.2	.8±.2

Table IV. Optical parameters, and radial parameters obtained by optical-model fits at each energy.

T_π (MeV)	$Reb_0(F^3)$	$Imb_0(F^3)$	$Reb_1(F^3)$	$Imb_1(F^3)$	a(F)	$R_c(F)$	$R_\pi(F)$	χ^2 (D/A)	χ^2 (av)	χ^2	χ^2 exptd.	Phase-shift method R_π	χ^2 exptd.	χ^2
51.3	-2.94±.10	.099±.28	5.83±.30	.100±.40	1.25±.04	2.37±.30	2.39±.45	16.7	23.8	40.5	24		16	34.9
59.7	-2.63±.09	-.165±.17	5.96±.20	.167±.25	1.26±.04	2.37±.18	2.39±.27	39.2	53.9	93.1	24	2.96±.43	16	85.8
67.6	-2.26±.11	-.568±.19	6.10±.30	.797±.39	1.19±.04	2.13±.33	2.02±.52	27.2	25.1	52.3	24		16	39.1
75.0	-2.18±.11	-.480±.18	6.22±.24	.567±.35	1.20±.04	2.38±.28	2.40±.42	28.6	29.5	58.1	24		16	52.1

Table V. Error matrix for best fit at 60 MeV.

	Reb_0	Imb_0	Reb_1	Imb_1	a_N	R_c
Reb_0	1.5×10^{-4}	-1.4×10^{-4}	-4.4×10^{-4}	1.6×10^{-4}	1.4×10^{-4}	3.4×10^{-4}
Imb_0		5.8×10^{-4}	-7.8×10^{-4}	-1.6×10^{-3}	-9.9×10^{-5}	-8.7×10^{-4}
Reb_1			5.5×10^{-3}	4.3×10^{-3}	-6.6×10^{-4}	3.6×10^{-4}
Imb_1				6.3×10^{-3}	-8.7×10^{-5}	2.4×10^{-3}
a_N					1.6×10^{-4}	3×10^{-4}
R_c						5.8×10^{-3}

Table VI. Distortion amplitudes. See text for more detailed assumptions for each method.

	Re	Im	$R_\pi^2(F^2)$	$R_\pi(F)$	χ^2	$\chi^2_{expected}$
	Method of Auerbach et al., Kisslinger model, 60-MeV data					
S	-0.0024 ± .0007	-0.010 ± .0011				
P	-0.0063 ± .0010	-0.008 ± .0009	8.29	2.88 ± 0.37	18.4	4
D	-0.0021 ± .0008	-0.003 ± .0009				
	Method of West, 60-MeV data					
S	0.00739	-0.00754				
P	-0.01114	0.00097	-0.27	<1.20 (1 s.d.)	84.0	4
D	-0.00243	-0.00010		<1.77 (2 s.d.)		
	Block integral Kisslinger model, 60-MeV data					
S	-0.00177	-0.00081				
P	-0.00566	-0.00138	5.11	2.26 ± 0.16	6.6	4
D	-0.00180	0.00113				
	Block integral and local potentials, 60-MeV data					
S	0.00215	-0.00015				
P	-0.01167	-0.00100	1.66	1.29 ± 0.82	76.1	4
D	-0.00271	0.00203				
	Block integral and local potentials, Block's 58-MeV data					
S	0.0033	-0.014				
P	-0.0141	0.0038	-0.4	< 0.9 (1 s.d.), <2.1 (2 s.d.)		
D	-0.0019	0.0025				

Figure Captions

Fig. 1. Layout of the pion beam line.

Fig. 2. Range curve for π^- obtained in the scattered beam (data from 70 and 75 deg combined).

Fig. 3. Pulse-height spectra obtained in the scattered beam at 70 deg for (a) 54-MeV π^+, (b) 60-MeV π^+, (c) 75-MeV π^+, (d) 60-MeV π^-. Empty target background has been subtracted. Typical error bars are shown. The solid curves are the best fit of two Gaussian curves to the experimental distribution.

Fig. 4. Elastic differential cross sections for πp at 60 MeV for (a) π^+, (b) π^-. The solid curves are the differential cross sections from the phase shifts of Ref. 15.

Fig. 5. Cross sections for (a) π^+ and (b) π^- at 60 MeV with best phase-shift fits, and (c) average cross section with best optical-model fit.

Fig. 6. D/A as a function of $\cos\theta_{c.m.}$, with best optical-model fits.

Fig. 7. The quantities -A and B are plotted vs $\cos\theta_{c.m.}$ for 60 MeV (see Eq. 2). The data points represent -A. The shaded area represents B with its uncertainty.

Fig. 8. (a) F_π plotted vs q^2. Best-fit curve is shown together with displacements of data points caused by shifting relative $\pi^+ - \pi^-$ normalization by its error.

(b) R_π vs q^2 for both extrema of the relative normalization. Two points at the largest value of q^2 are missing because they are not real. The best-fit value and error are plotted for reference.

Fig. 9. Feynman diagrams not taken into account by the optical model.

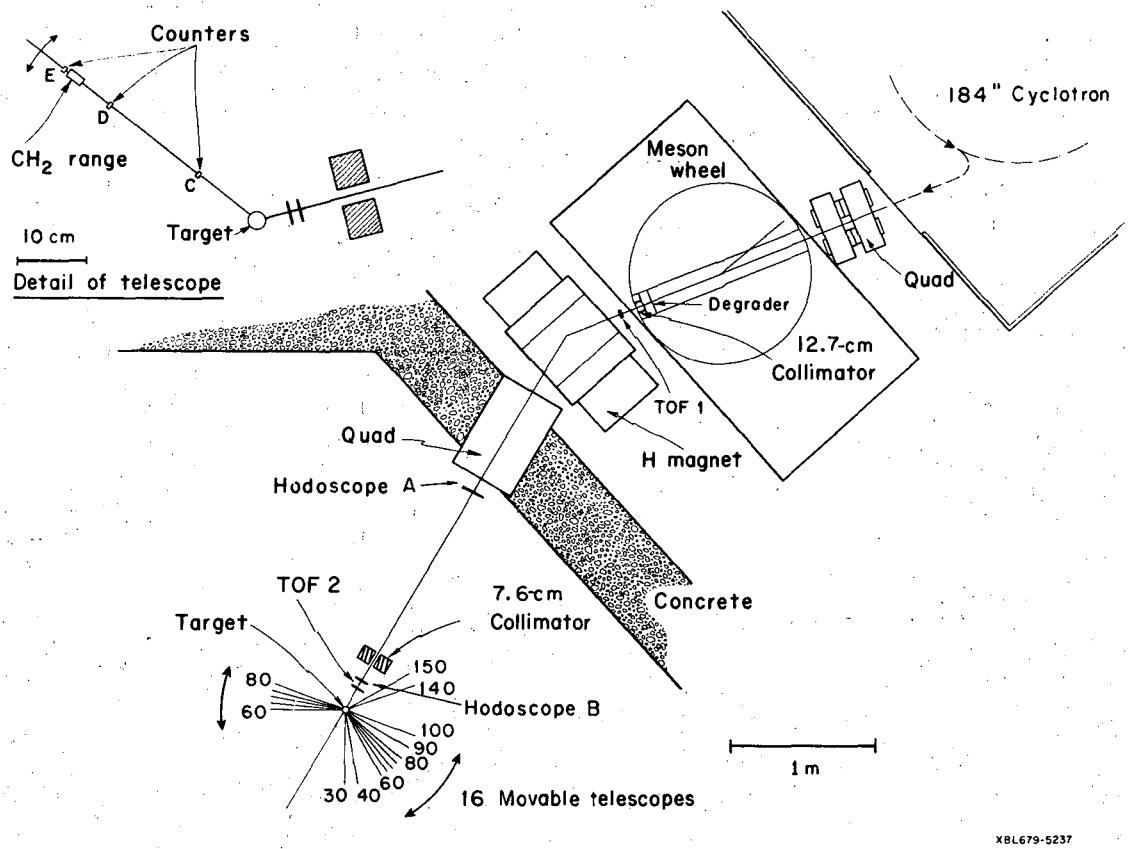
Counters
E
D
CH_2 range
C
Target
10 cm
Detail of telescope
184" Cyclotron
Meson wheel
Quad
Degrader
12.7-cm Collimator
TOF 1
H magnet
Quad
Hodoscope A
TOF 2
Target
7.6-cm Collimator
Concrete
80
60
150
140
Hodoscope B
100
90
80
60
30 40
16 Movable telescopes
1 m
XBL679-5237

Fig. 1

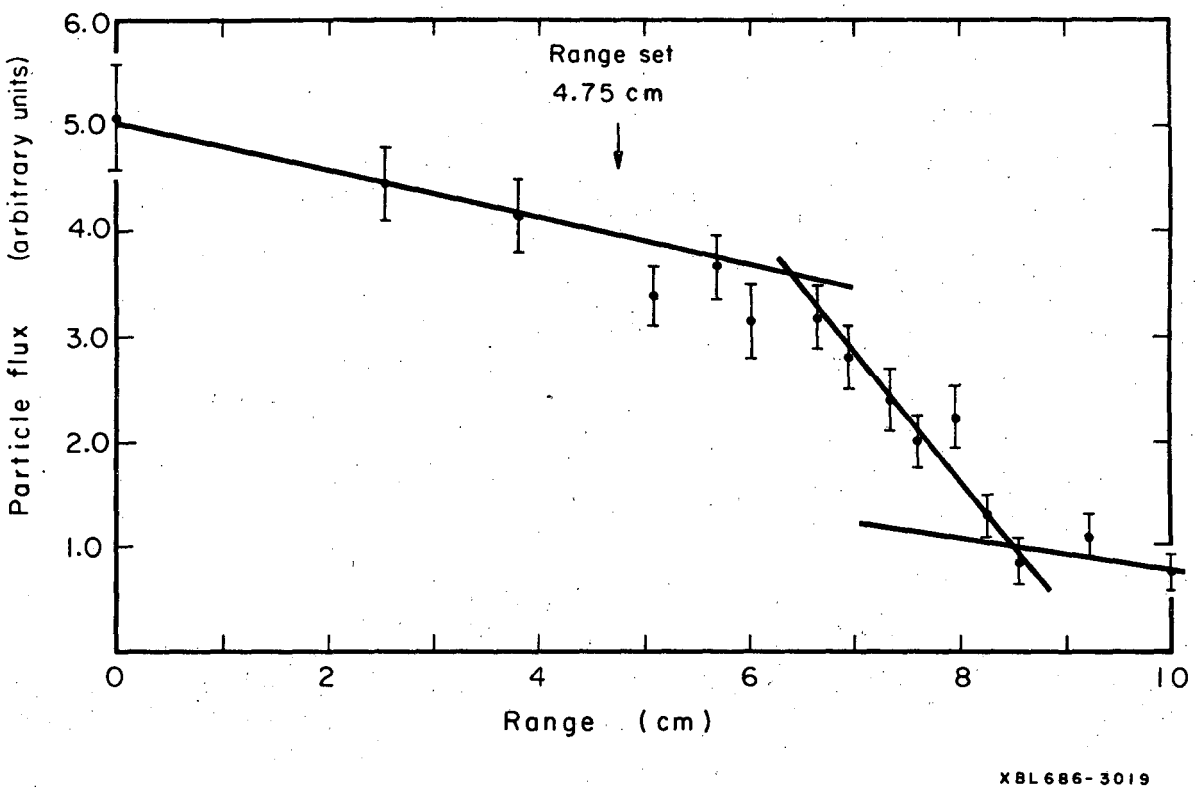
Range set
4.75 cm
Particle flux (arbitrary units)
6.0
5.0
4.0
3.0
2.0
1.0
0
2
4
6
8
10
Range (cm)
XBL686-3019

Fig. 2

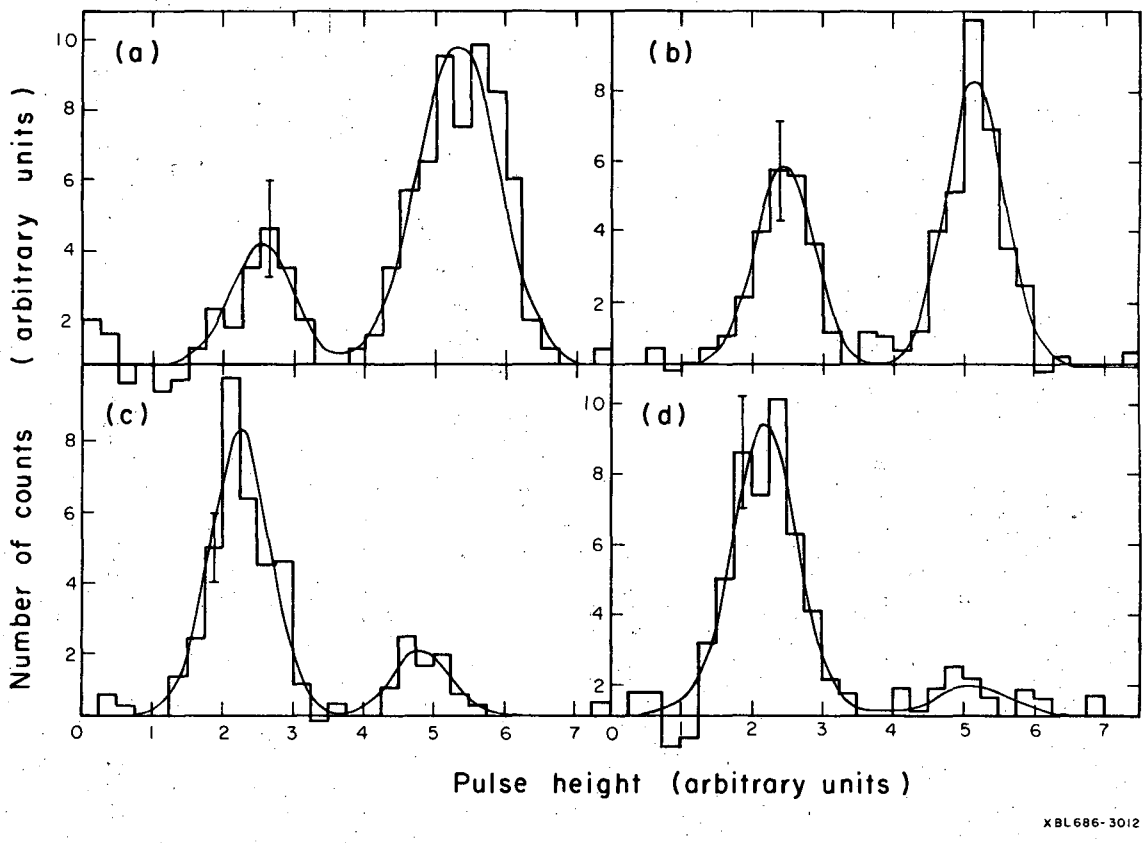
(a)
(b)
(c)
(d)
Number of counts (arbitrary units)
Pulse height (arbitrary units)
XBL686-3012

Fig. 3

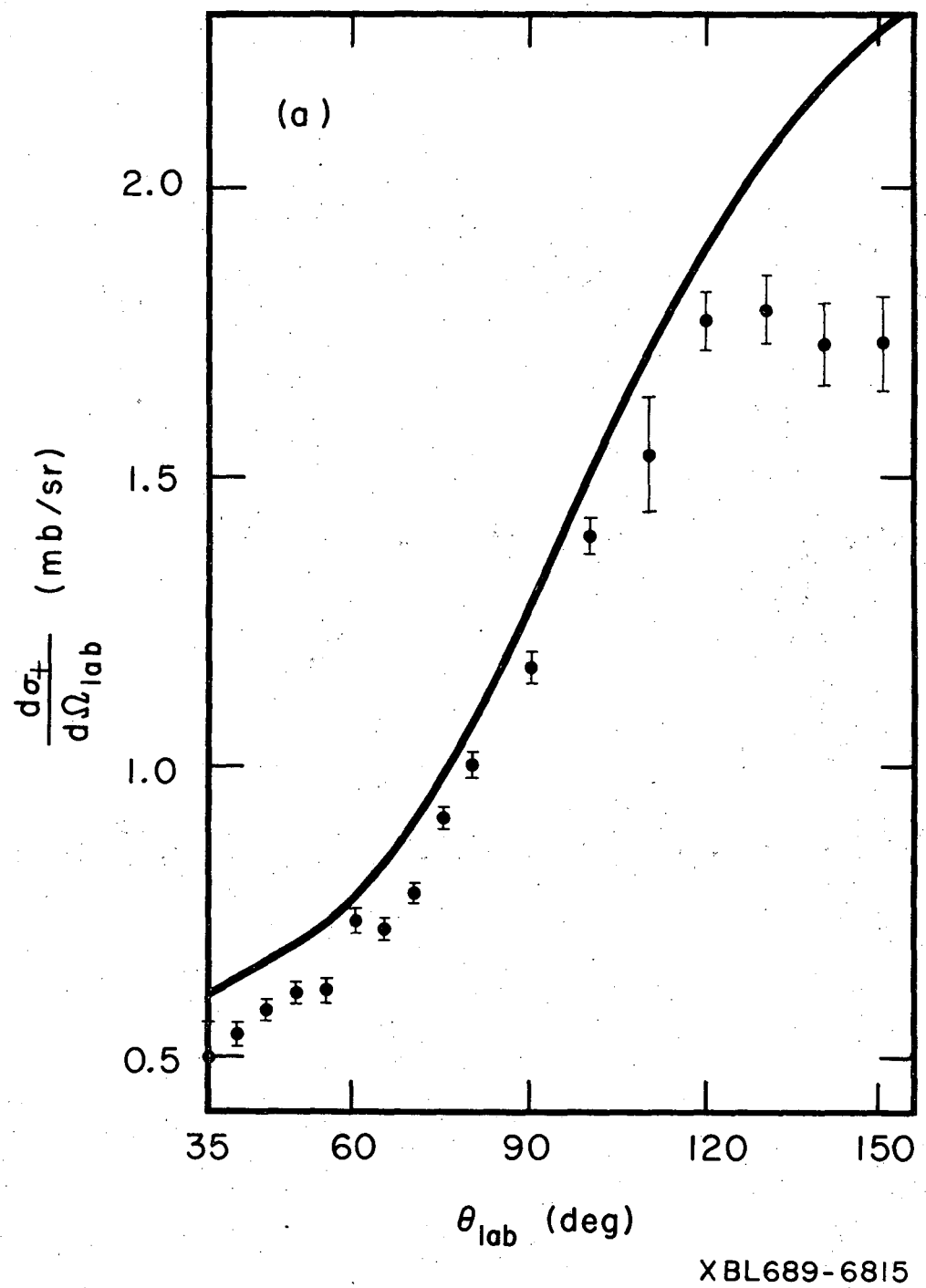
(a)
2.0
1.5
1.0
0.5
$\frac{d\sigma_+}{d\Omega_{lab}}$ (mb/sr)
35
60
90
120
150
θ_{lab} (deg)
XBL689-6815

Fig. 4a

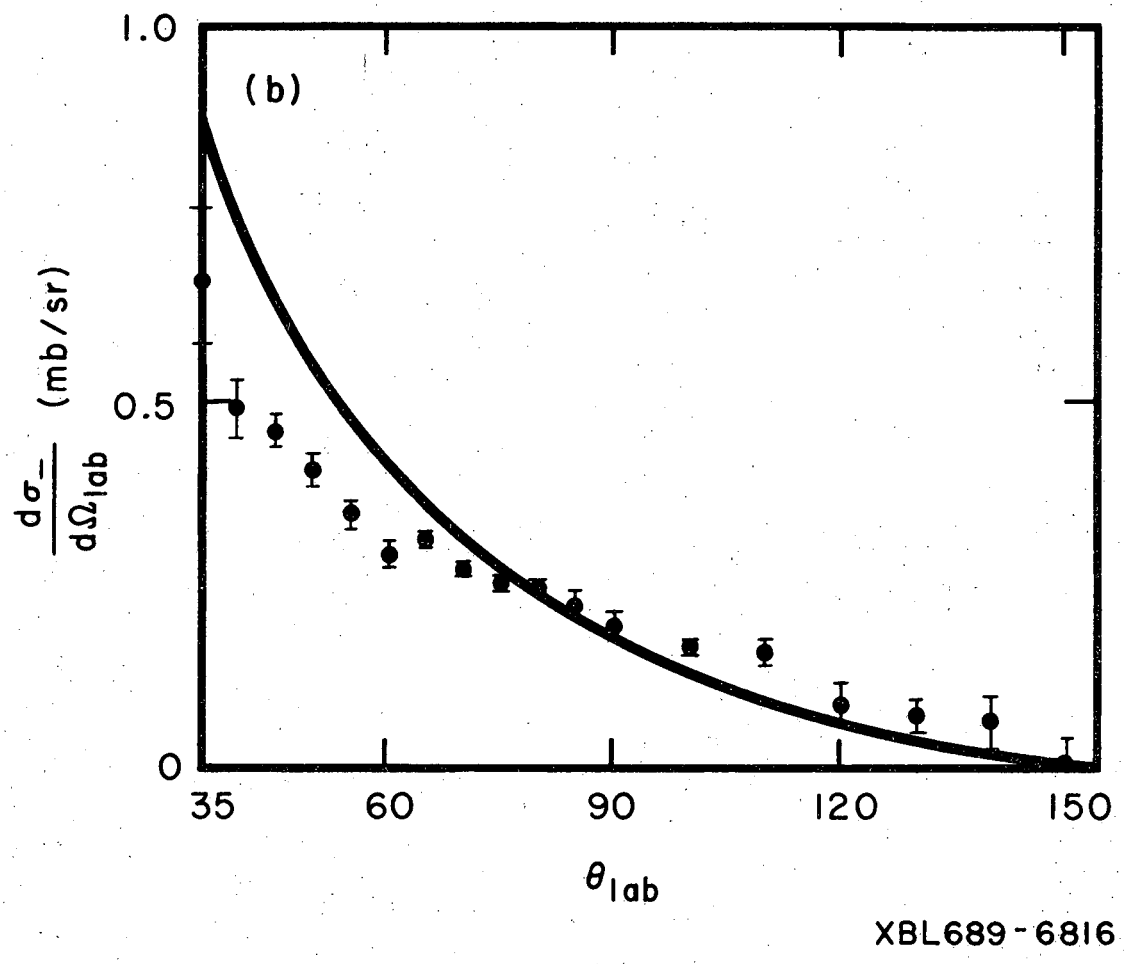
1.0
(b)
0.5
0
$\frac{d\sigma_-}{d\Omega_{lab}}$ (mb/sr)
35
60
90
120
150
θ_{lab}
XBL689-6816

Fig. 4b

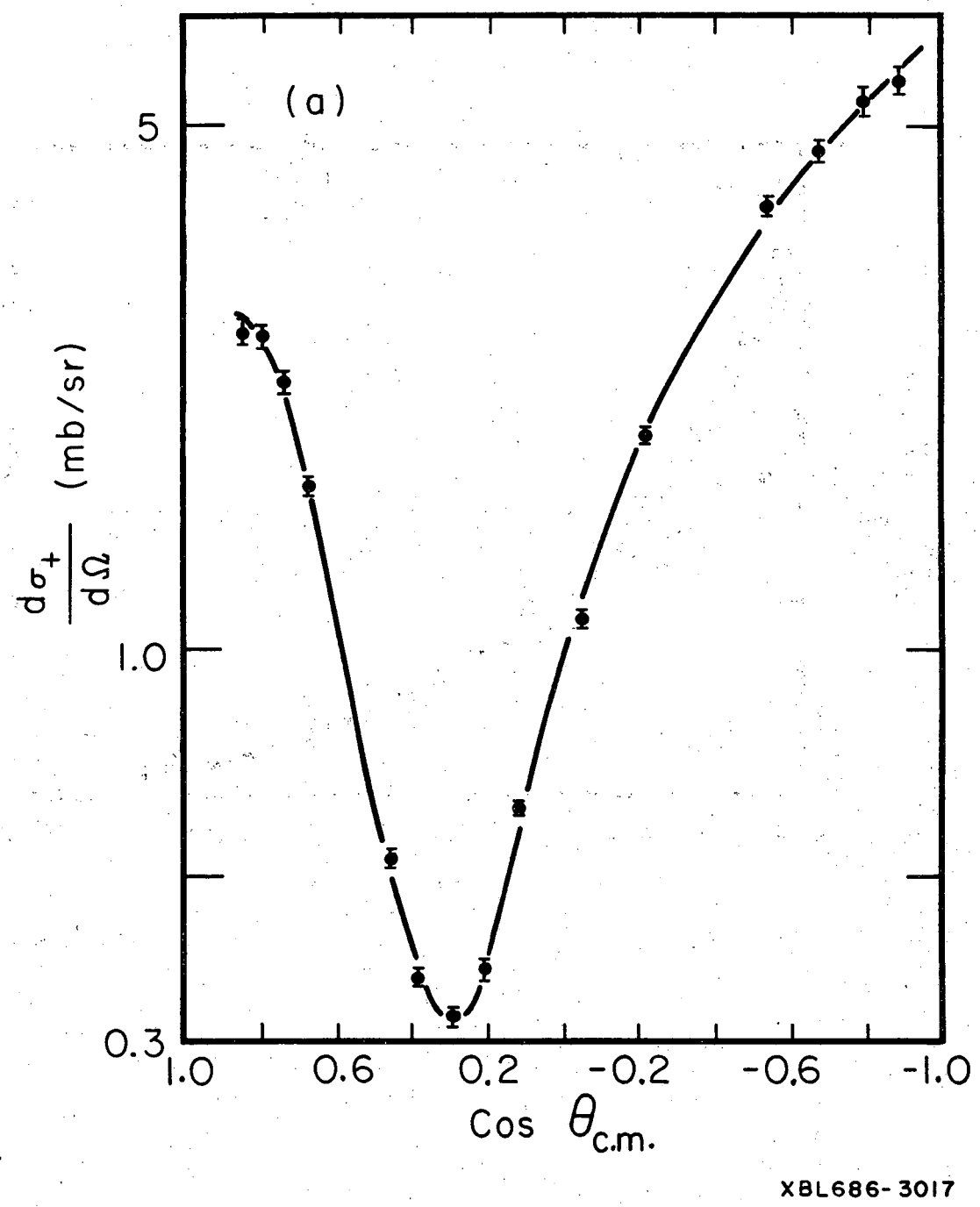
(a)
5
1.0
0.3
$\frac{d\sigma_+}{d\Omega}$ (mb/sr)
1.0
0.6
0.2
-0.2
-0.6
-1.0
Cos $\theta_{c.m.}$
XBL686-3017

Fig. 5a

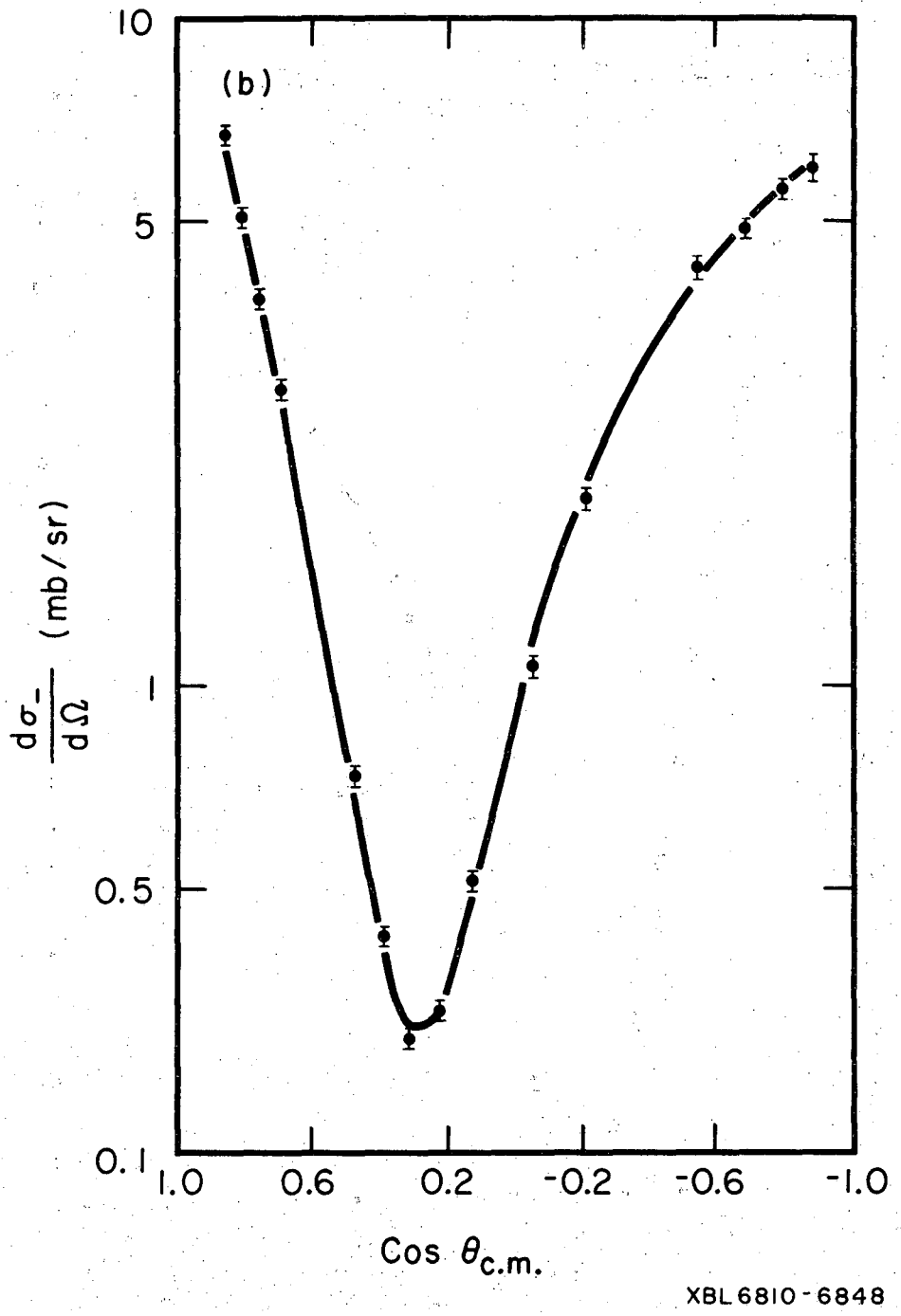
(b)
10
5
1
0.5
0.1
$\frac{d\sigma_-}{d\Omega}$ (mb/sr)
1.0
0.6
0.2
-0.2
-0.6
-1.0
Cos $\theta_{c.m.}$
XBL6810-6848

Fig. 5b

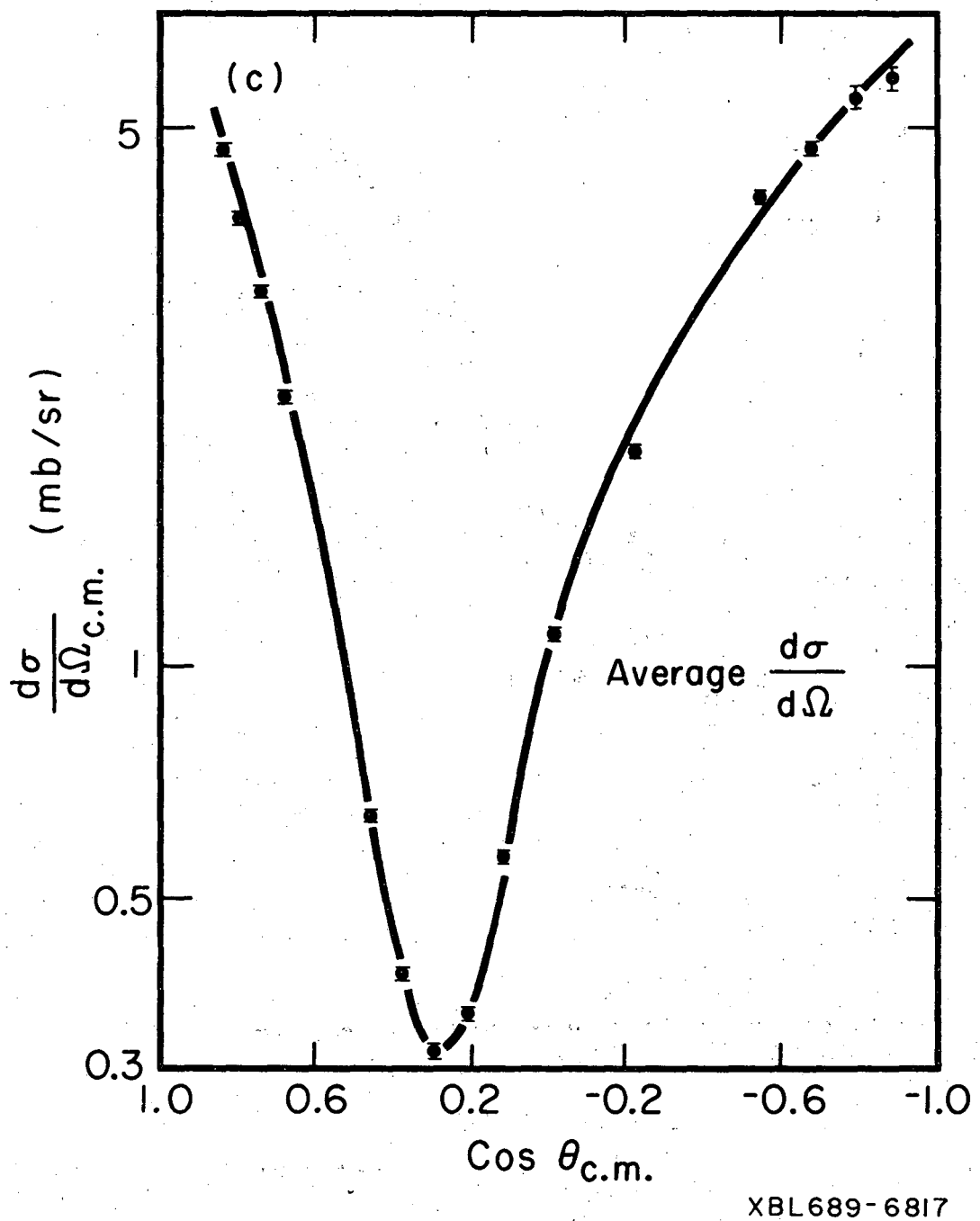
(c)
5
1
0.5
0.3
$\frac{d\sigma}{d\Omega_{c.m.}}$ (mb/sr)
Average $\frac{d\sigma}{d\Omega}$
1.0
0.6
0.2
-0.2
-0.6
-1.0
Cos $\theta_{c.m.}$
XBL689-6817

Fig. 5c

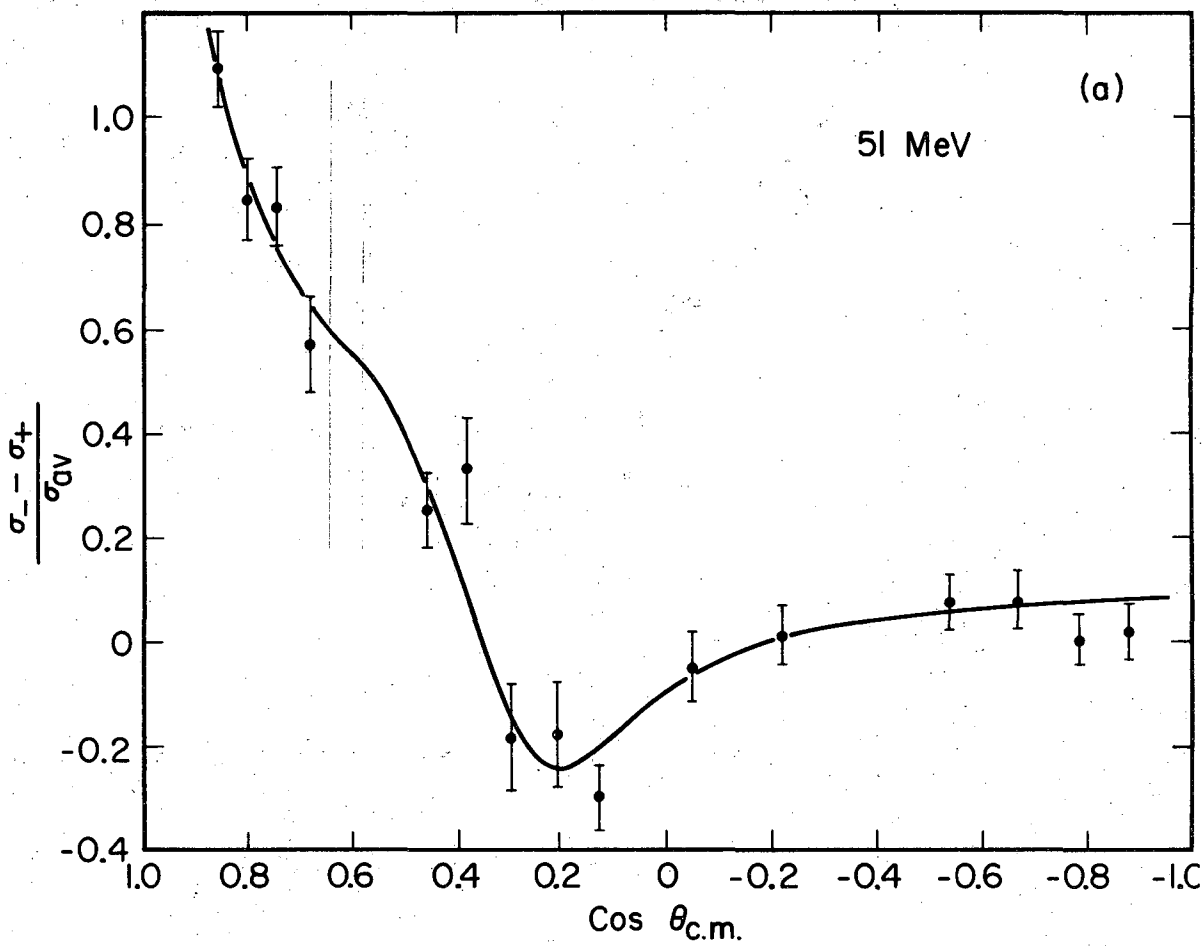

XBL686-3013

Fig. 6a

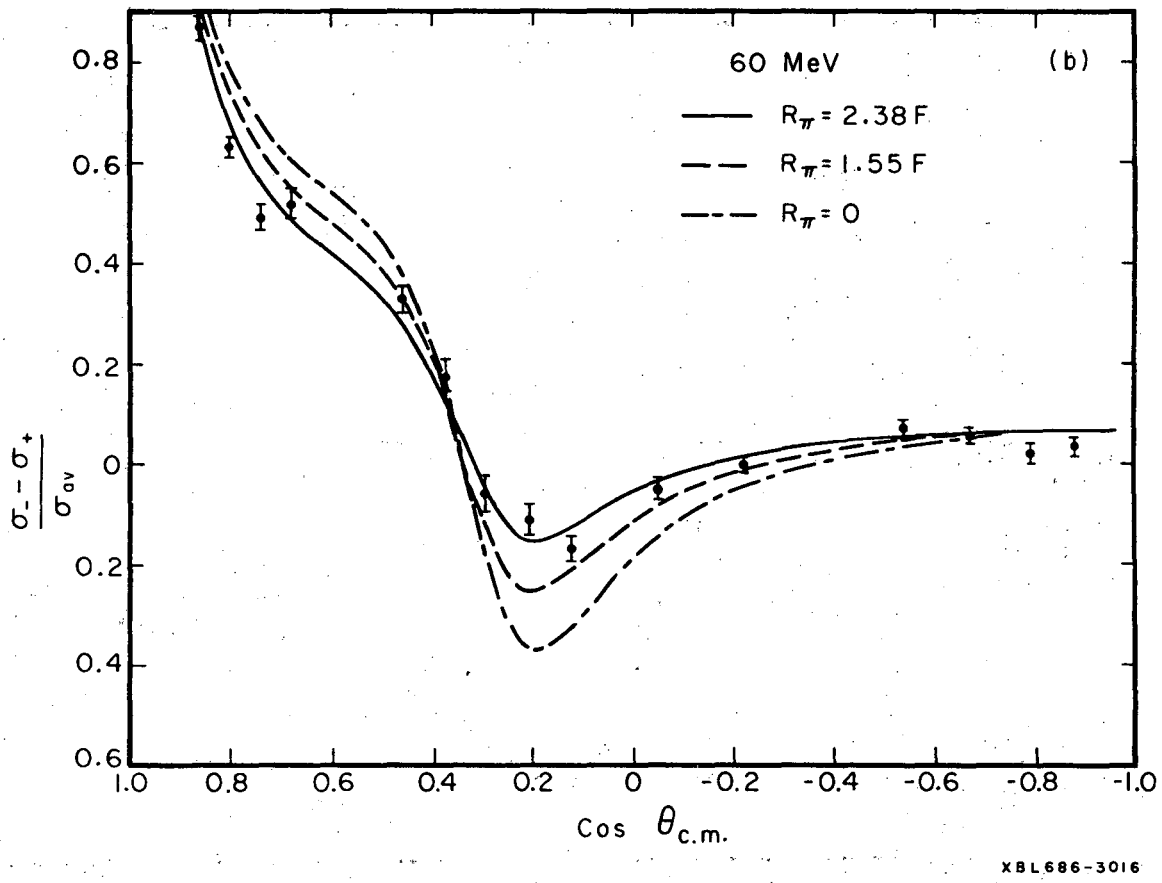
60 MeV
(b)
R_π = 2.38 F
R_π = 1.55 F
R_π = 0
$\frac{\sigma_- - \sigma_+}{\sigma_{av}}$
0.8
0.6
0.4
0.2
0
0.2
0.4
0.6
1.0
0.8
0.6
0.4
0.2
0
-0.2
-0.4
-0.6
-0.8
-1.0
Cos $\theta_{c.m.}$
XBL686-3016

Fig. 6b

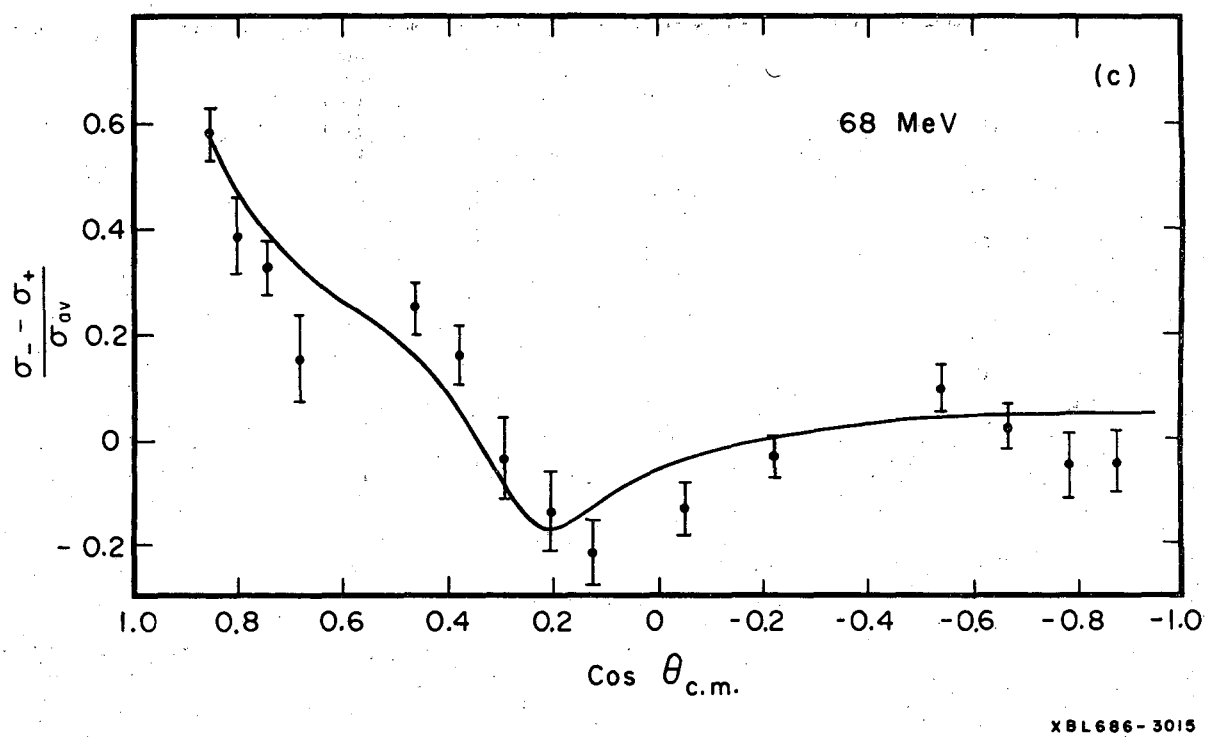
(c)
68 MeV
0.6
0.4
0.2
0
-0.2
$\frac{\sigma_- - \sigma_+}{\sigma_{av}}$
1.0
0.8
0.6
0.4
0.2
0
-0.2
-0.4
-0.6
-0.8
-1.0
Cos $\theta_{c.m.}$
XBL686-3015

Fig. 6c

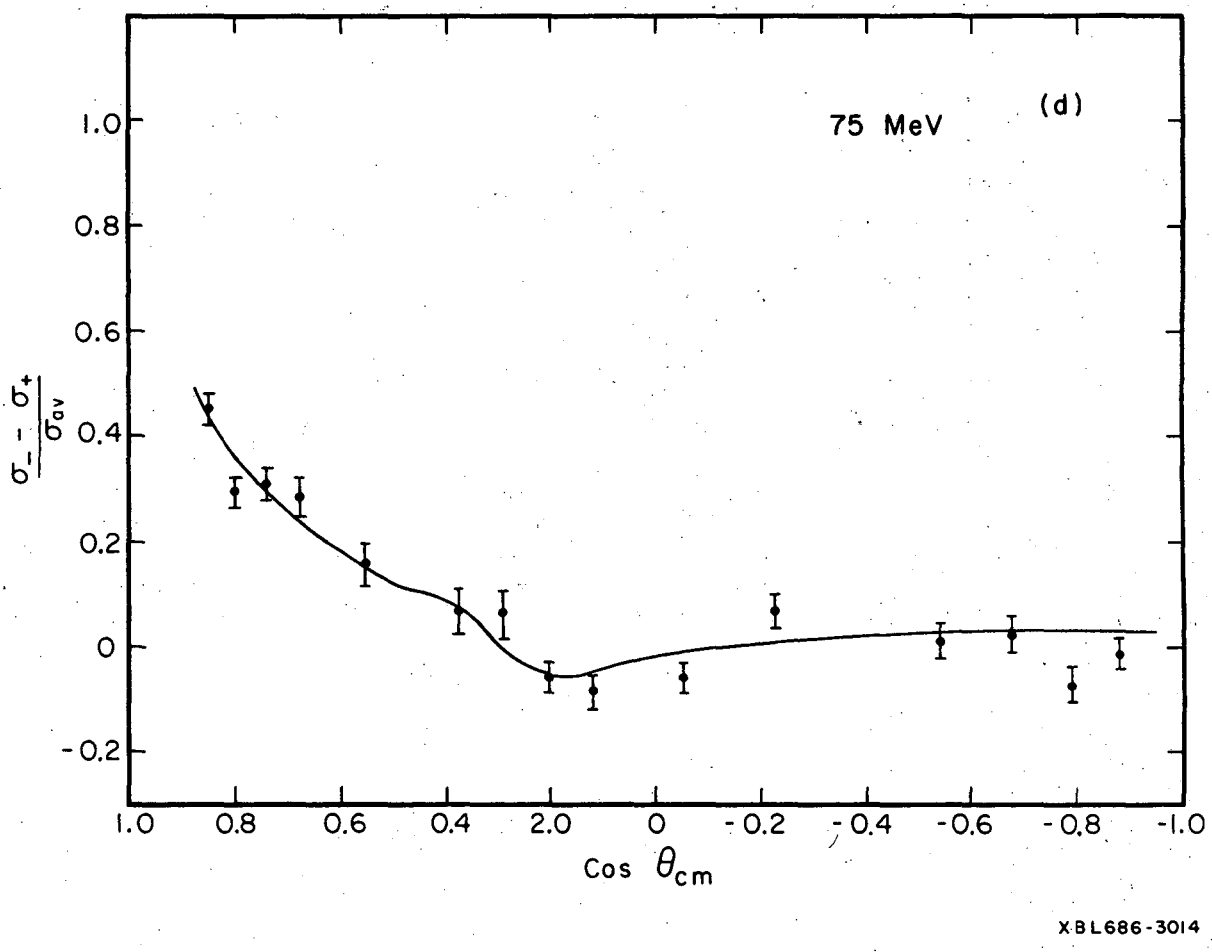
75 MeV
(d)
1.0
0.8
0.6
0.4
0.2
0
-0.2
$\frac{\sigma_- - \sigma_+}{\sigma_{av}}$
1.0
0.8
0.6
0.4
2.0
0
-0.2
-0.4
-0.6
-0.8
-1.0
Cos θ_{cm}
XBL686-3014

Fig. 6d

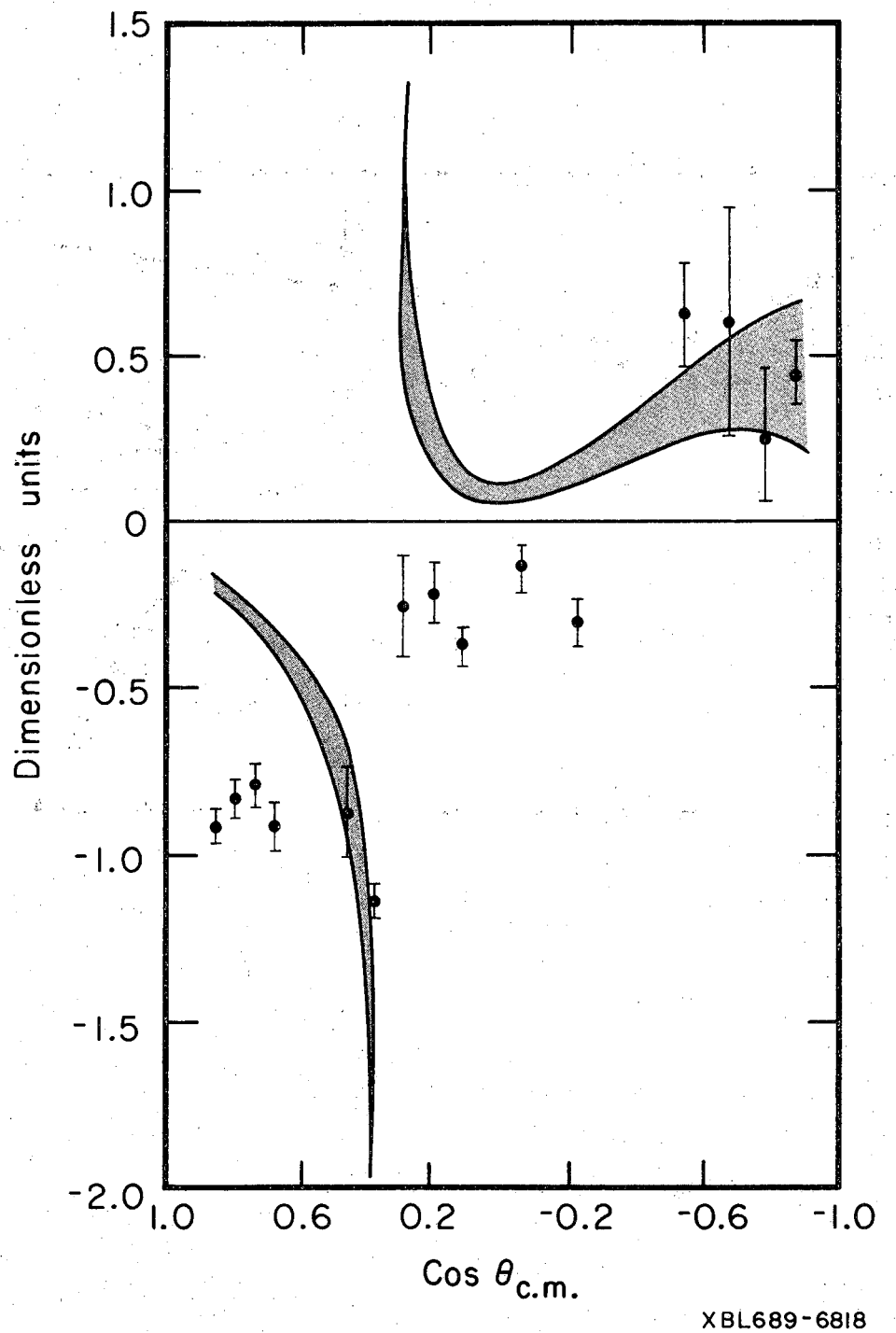
1.5
1.0
0.5
0
-0.5
-1.0
-1.5
-2.0
Dimensionless units
1.0
0.6
0.2
-0.2
-0.6
-1.0
Cos θc.m.
XBL689-6818

Fig. 7

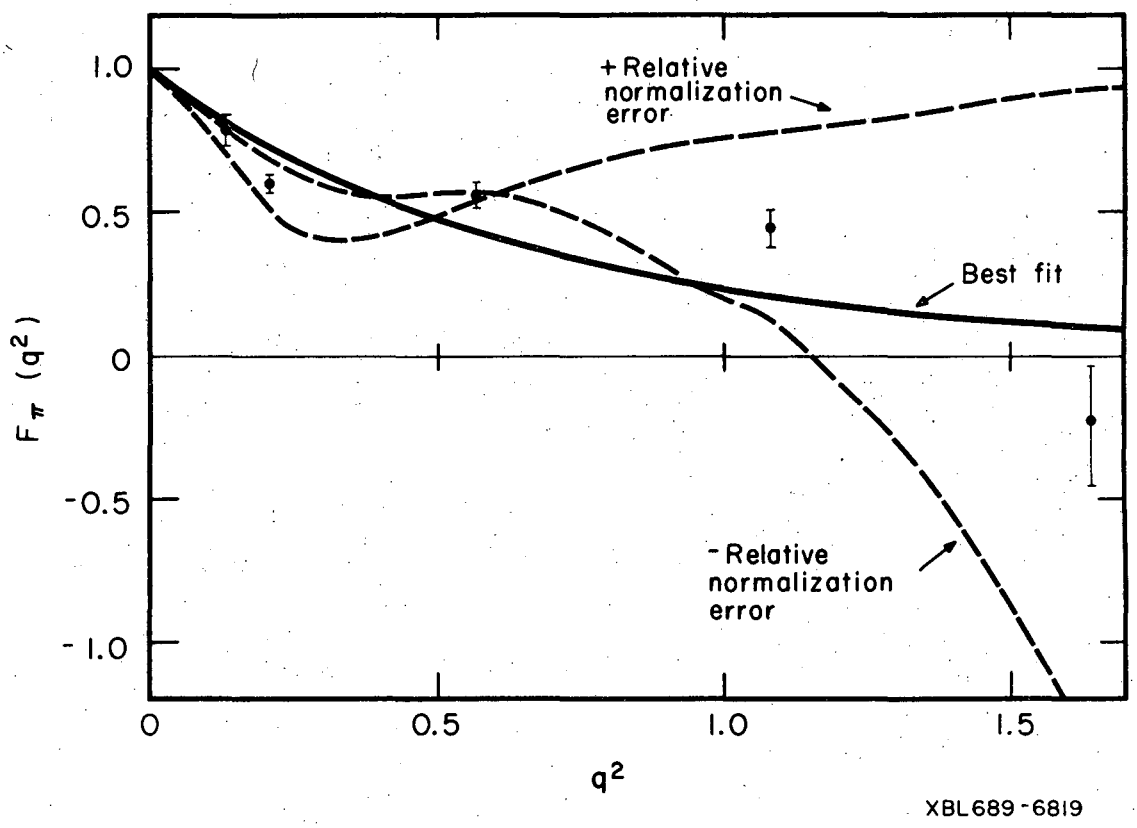
1.0
0.5
0
-0.5
-1.0
0
0.5
1.0
1.5
F_π (q^2)
q^2
+ Relative normalization error
Best fit
- Relative normalization error
XBL689-6819

Fig. 8a

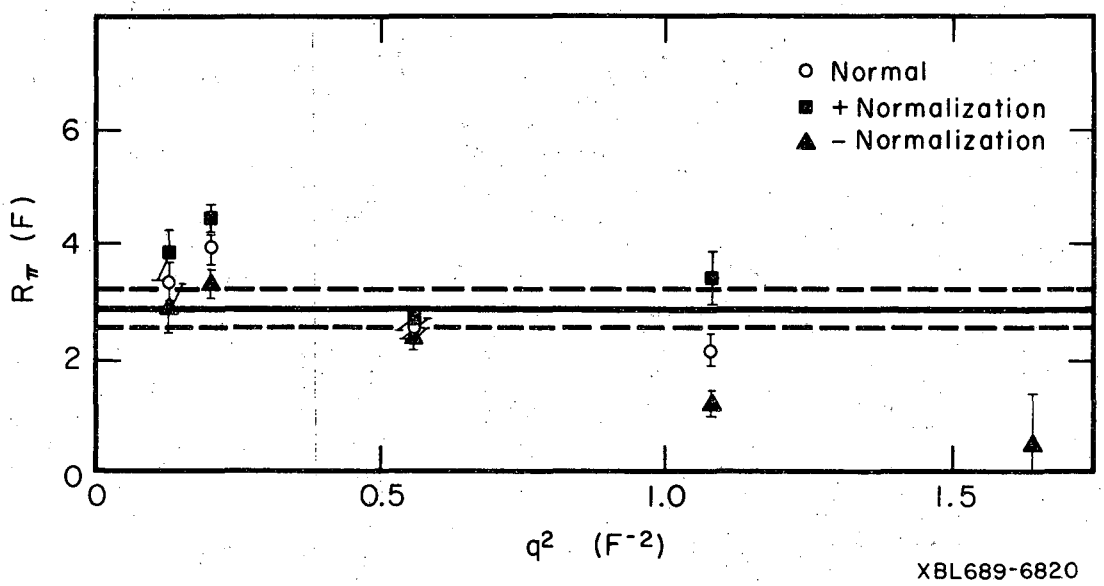
Normal
+ Normalization
- Normalization
R_π (F)
0
2
4
6
0
0.5
1.0
1.5
q^2 (F^{-2})
XBL689-6820

Fig. 8b

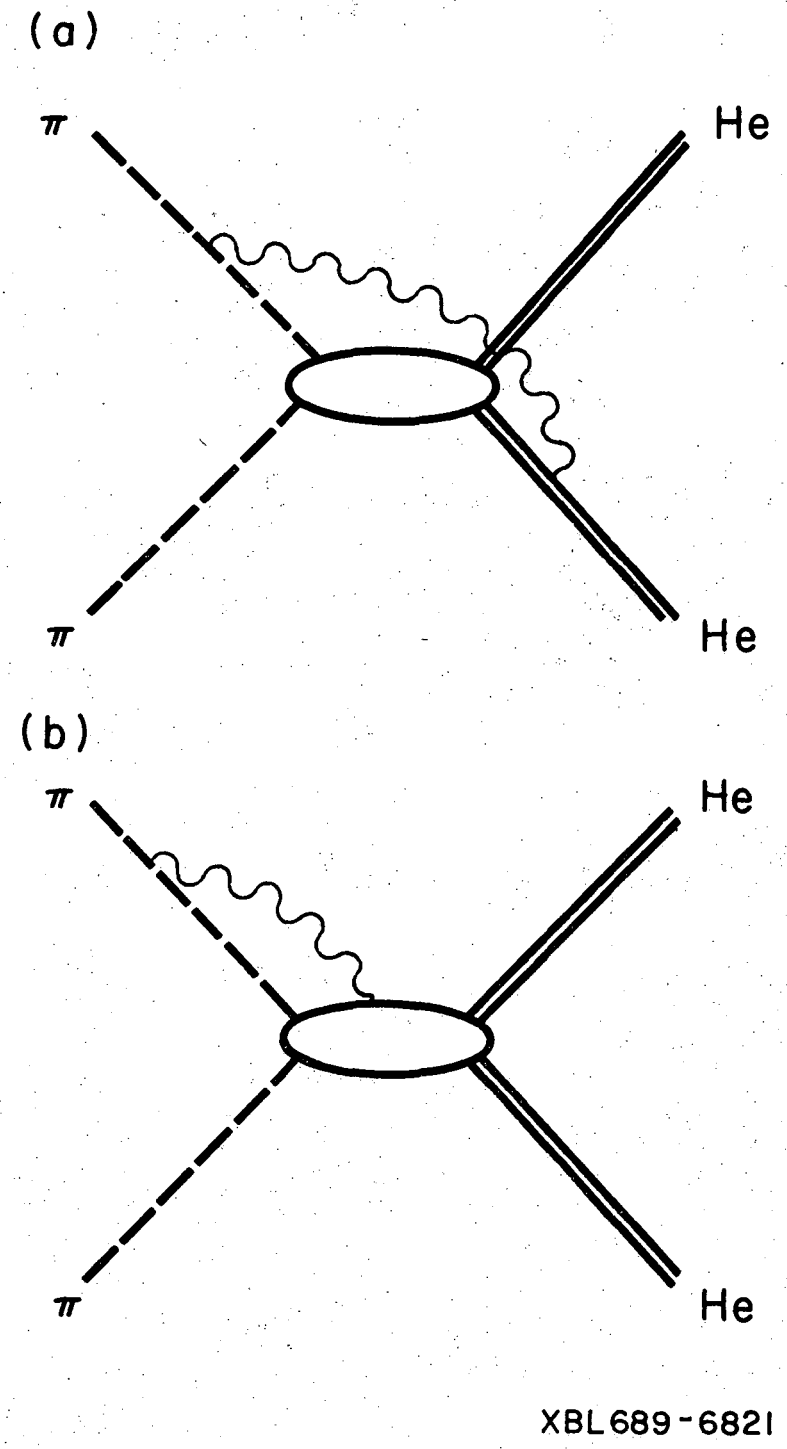

Fig. 9

LEGAL NOTICE

TECHNICAL INFORMATION DIVISION
LAWRENCE RADIATION LABORATORY
UNIVERSITY OF CALIFORNIA
BERKELEY, CALIFORNIA 94720